# Microwave Holography for EMI Source Imaging

Xin Yan , *Member, IEEE*, Jiangshuai Li, *Member, IEEE*, Wei Zhang, *Member, IEEE*, Kaustav Ghosh, Philippe Sochoux, Daryl G. Beetner, *Fellow, IEEE*, and Victor Khilkevich, *Senior Member, IEEE* 

Abstract—Emission source microscopy technique can be utilized to localize the radiation sources in complex and electrically large electronic systems. In the two-dimensional emission source microscopy algorithm, both magnitude and phase of the field need to be measured, and a vector network analyzer or an oscilloscope has to be used as a receiver, resulting in reduced signal-to-noise ratio and longer measurement time compared to a spectrum analyzer (SA). In this article, a phaseless electromagnetic interference source imaging method is proposed based on microwave holography. The field produced by the device under test is not measured directly, instead, the interference pattern between the emitted field and the reference wave is created and measured as the hologram. The hologram is a real-valued function that can be measured using a SA. The proposed method is validated through measurements for both passive and active devices. The proposed algorithm is efficient and reliable in identifying major radiation sources and determining their location and relative strength.

*Index Terms*—Emission source microscopy, microwave holography, radiation sources, source imaging.

#### I. INTRODUCTION

ITH increasing of the operating data rate in electronic devices, electromagnetic interference (EMI) issues are becoming more critical for complex and large systems. For instance, the optical modules used in network equipment could cause EMI problems at frequencies up to tens of GHz [1]. To identify the radiating sources of the EMI that contribute to the far-field region, the emission source microscopy (ESM) technique could be used by measuring the field over a plane at an electrically large distance from the device under test (DUT) and back-propagating the field onto the DUT plane.

In previous works, the 2-D ESM algorithm was derived [2], [3]. The uniformly distributed scanning points are picked on the scan plane with the separation between the points less than  $\lambda/2$  in order to satisfy the Nyquist spatial sampling criterion. In [4], the sparse emission source microscopy was proposed to minimize the number of required spatial samples.

Manuscript received 1 April 2023; revised 25 July 2023 and 19 October 2023; accepted 15 November 2023. Date of publication 19 December 2023; date of current version 16 April 2024. This work was supported in part by the National Science Foundation under Grant IIP-1916535. (Corresponding author: Victor Khilkevich.)

Xin Yan, Jiangshuai Li, Wei Zhang, Daryl G. Beetner, and Victor Khilkevich are with the Electromagnetic Compatibility Laboratory, Missouri University of Science and Technology, Rolla, MO 65409 USA (e-mail: yx9n9@mst.edu; lijiangs@mst.edu; wznkm@mst.edu; daryl@mst.edu; khilkevichv@mst.edu).

Kaustav Ghosh and Philippe Sochoux are with the Juniper Networks Company, Sunnyvale, CA 94089 USA (e-mail: kvghosh@juniper.net; pso-choux@juniper.net).

Color versions of one or more figures in this article are available at https://doi.org/10.1109/TEMC.2023.3340233.

Digital Object Identifier 10.1109/TEMC.2023.3340233

Another sparse ESM scan using Gaussian process regression was proposed in [5]. In [6], the effects on image quality of different scanning point selection methods were analyzed.

The ESM algorithm has been analyzed and optimized by researchers, however, the method requires to measure both the magnitude and phase of the field and a vector network analyzer (VNA) or an oscilloscope has to be used as a receiver, resulting in a relatively low signal-to-noise ratio and long measurement time (due to a relatively slow sweep of the VNAs and a large amount of the data needed to be collected in the time-domain measurement to achieve high frequency resolution). These deficiencies of the traditional 2-D ESM algorithm have significant impact on the applicability of the method in cases of weak radiation sources.

Holography is an imaging technique used to reconstruct the object wavefront (i.e., the wavefront scattered or produced by the object) from the recording of an interference pattern created by an object beam and a reference beam. This technique was originally introduced by Gabor to increase the resolution of electron microscopes [7] and later extended to the microwave field [8]. The interference pattern, known as the hologram, is a real-valued function, which can be measured by a spectrum analyzer (SA), alleviating the deficiencies of the traditional imaging technique outlined above. An example of the phaseless antenna diagnostics based on the microwave holography was presented in [9].

In this article, we propose a phaseless EMI source imaging method based on microwave holography, which is an alternative solution for localization and characterization of active radiation sources. The hologram is created by combining the field from the scan antenna with a reference signal collected by the second antenna placed near the DUT and naturally producing a much stronger signal than the scan antenna. The normalized hologram is backpropagated to the source plane and the image of sources is obtained. The proposed method is validated through measurements in which the radiation sources are visualized and localized successfully.

The rest of this article is organized as follows. Section II presents the analytical formulation of the microwave holography imaging methodology. The measurement setup and results are demonstrated in Section III. Finally, Section IV concludes this article.

## II. MICROWAVE HOLOGRAPHY IMAGING ALGORITHM

## A. Two-Dimensional ESM Algorithm

The 2-D ESM algorithm is based on the synthetic aperture radar technique, and a typical implementation of the method is

0018-9375 © 2023 IEEE. Personal use is permitted, but republication/redistribution requires IEEE permission. See https://www.ieee.org/publications/rights/index.html for more information.

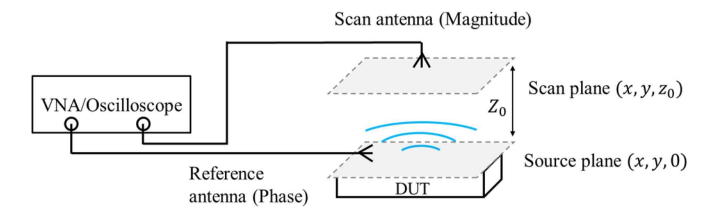


Fig. 1. Two-dimensional ESM setup.

illustrated by Fig. 1. The electric field on a plane with elevation 0 can be represented as a superposition of plane waves in the form of the Fourier transform [3]

$$E(x, y, 0) = \frac{1}{4\pi^2} \int_{-\infty}^{\infty} \int_{-\infty}^{\infty} f(k_x, k_y) e^{-j(k_x x + k_y y)} dk_x dk_y$$
(1)

where  $f(k_x,k_y)$  is spectrum of the field distribution, and  $k_x$  and  $k_y$  are the spatial frequencies in the x and y directions, respectively. The spectrum of the field on any plane  $(x,y,z_0)$  parallel to (x,y,0) can be found as

$$f(k_x, k_y, z_0) = f(k_x, k_y) \cdot e^{-jk_z z_0}$$
 (2)

where

$$k_z = \sqrt{k^2 - k_x^2 - k_y^2}, \quad \text{if } k_x^2 + k_y^2 \le k^2$$
 (3a)

$$k_z = -j\sqrt{k_x^2 + k_y^2 - k^2}$$
, otherwise. (3b)

In (3) k is the wavenumber, and  $k_z$  is the z component of the propagation vector. Real  $k_z$  corresponds to propagating components of the spectrum, while the imaginary values give the evanescent waves. Formulas (1) and (2) can be used to transform the field between any parallel planes. For example, if the field on the scanning plane  $(x, y, z_0)$  is known, the field on the DUT plane (x, y, 0) can be backpropagated as

$$E(x, y, 0) = \mathcal{F}^{-1}\left(\mathcal{F}\left[E(x, y, z_0)\right] e^{jk_z z_0}\right) \tag{4}$$

where  $\mathcal{F}$  and  $\mathcal{F}^{-1}$  are the forward and inverse Fourier operators, respectively. Equation (4) serves as the basis of the 2-D ESM algorithm.

### B. Hologram Formation and Reconstruction

In the field of optics and electron microscopy, it is impossible to measure the phase of the signal directly. The hologram provides a way to record and reproduce the field information by including the phase information as the magnitude variation of the interference pattern. Here, we explain the hologram formation and image reconstruction using in-line holography as an example. The diagram of the in-line holography is shown in Fig. 2 [10].

Consider a plane wave R passing by an object located on the plane (x, y, 0). Part of the wave is scattered by the object, which creates the object wave O. The two waves interfere beyond the object and the power of the interference pattern U = R + O is recorded at some distance  $z_0$ , i.e., at the hologram plane  $(x, y, z_0)$ . The recorded hologram  $H(x, y, z_0)$ , therefore,

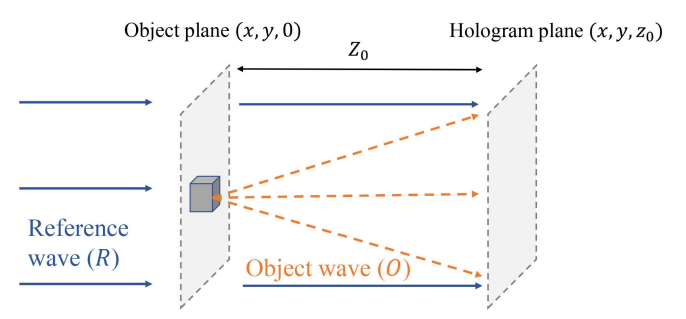


Fig. 2. In-line holography diagram.

is given by

$$H(x, y, z_0) = |U(x, y, z_0)|^2 = |R(x, y, z_0)|^2 + |O(x, y, z_0)|^2 + R^*(x, y, z_0) O(x, y, z_0) + O^*(x, y, z_0) R(x, y, z_0)$$
(5)

where  $|R(x,y,z_0)|^2$  is the power of the reference wave, and  $|O(x,y,z_0)|^2$  is the power of the scattered wave. The last two terms are the interference pattern observed in the hologram. For successful imaging, it is required that the power of the reference wave is much larger than the power of the object wave, i.e.,  $|R|^2 \gg |O|^2$ . Under this condition the hologram is approximated as

$$H(x, y, z_0) \approx |R(x, y, z_0)|^2 + R^*(x, y, z_0) O(x, y, z_0) + O^*(x, y, z_0) R(x, y, z_0).$$
 (6)

Before generating the image, the hologram is normalized as

$$H_{0}(x, y, z_{0}) = \frac{H(x, y, z_{0})}{|R(x, y, z_{0})|^{2}} - 1 \approx \frac{R^{*}(x, y, z_{0}) O(x, y, z_{0})}{|R(x, y, z_{0})|^{2}} + \frac{O^{*}(x, y, z_{0}) R(x, y, z_{0})}{|R(x, y, z_{0})|^{2}}.$$
 (7)

The normalized hologram is then backpropagated to produce the normalized image on the source/object plane using the same transformation as in (4)

$$I_0(x, y, 0) = \mathcal{F}^{-1}(\mathcal{F}[H_0(x, y, z_0)]e^{jk_z z_0}).$$
 (8)

The intensity of the image  $I_0$  is given relative to the intensity of the reference wave  $R(x,y,z_0)$ . To obtain the absolute values of the image intensity, the normalized image needs to be multiplied by  $|R(x,y,z_0)|$ .

## C. Twin Object Effect

As the 2-D ESM algorithm uses both the magnitude and phase of the scanned field, the resulting image is free of any artifacts other than those related to limited scan area (aperture diffraction) and sampling (aliasing). In holography, however, the interference pattern  $R^*O + O^*R$  is recorded, where the component proportional to O would produce the actual image of the object, and the component  $O^*$ , which is due to the imaginary object located on the opposite side of the hologram plane and emitting waves in the opposite direction relative to the actual

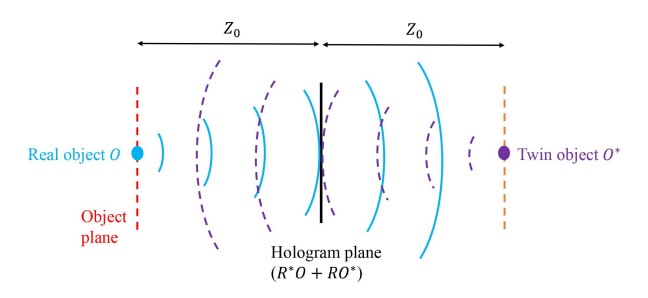


Fig. 3. Diagram of the twin object effect.

object (the complex conjugate in  $O^*$  reverses the propagation direction of all waves in the plane wave spectrum) would produce the twin image. The image of the twin object is always presented in holography and is especially detrimental for in-line measurement, as shown in Fig. 2. However, the effect of the twin object is mitigated as the distance between the actual object and the hologram plane is increased. A diagram of the twin object effect is shown in Fig. 3. The image at the object plane includes the focused image of the real object and the unfocused image of the twin object, which can be considered as noise added to the image.

To analyze the image quality, a hologram of a short dipole is calculated numerically. The frequency is set to 5 GHz, and the distance between the source and hologram planes is 0.5 m. The electric field generated by the dipole is calculated on a 2 m  $\times$  2 m hologram plane and a large (compared to the field values) constant is added to the field distribution to form the hologram.

The simulation results are shown in Fig. 4. The object and reference waves at the hologram plane (at z = 0.5 m) are shown in Fig. 4(a) and (b), respectively. The image in Fig. 4(c) represents the hologram. As can be seen, the hologram pattern has small variations of the magnitude relative to the value of the reference wave (less than 0.2 dB). The image at z = 0 m produced from the hologram is shown in Fig. 4(d). The point source is visualized and localized successfully. For comparison Fig. 4(e) and (f) shows the images from the real and twin object at the source plane, respectively. The holography image in Fig. 4(d) is a summation of the actual object [see Fig. 4(e)] and twin object [see Fig. 4(f)] images. As can be seen, the twin object significantly increases the amount of the background noise, but since the twin object is out of focus, the peak value of its image is more than 25 dB lower than the peak of the actual object image, which is sufficient for many practical applications. It is noticed that the twin object effect is influenced by the distance between the source plane and hologram plane. When the backpropagation distance is small, the twin image may be strong enough to cause considerable degradation of the object image, however, a proper selection of the distance between the object and hologram plane allows to decrease the contribution of the twin object to an acceptable level in many cases.

# D. Microwave Holography Imaging Algorithm

Optical holography is almost always performed by creating a physical reference wave using a laser source. A similar approach

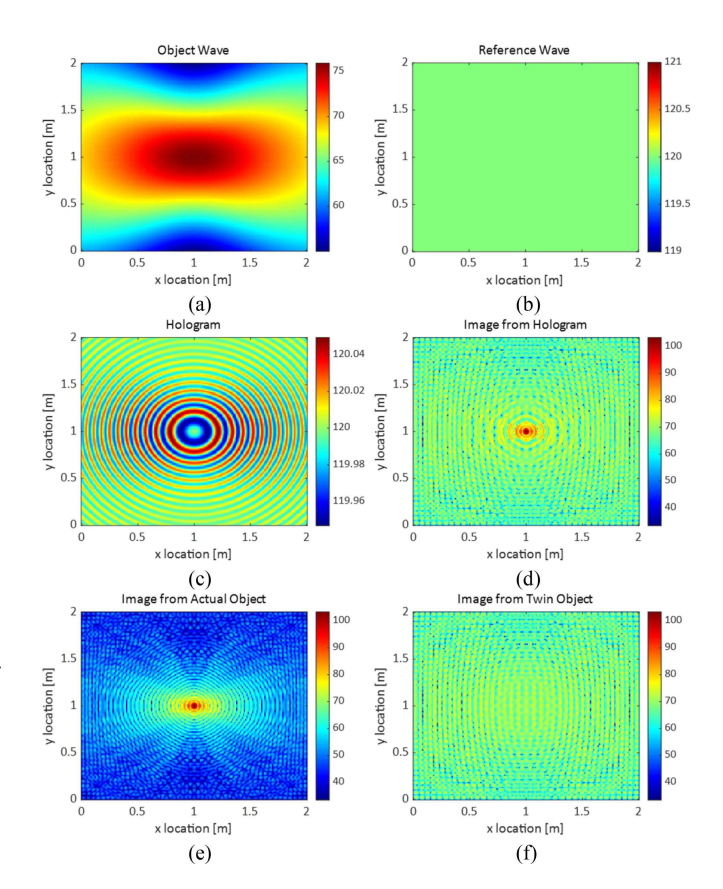


Fig. 4. Simulated imaging of a point source. The color scale represents the values in dB relative to 1 V/m. (a) Object wave at the hologram plane. (b) Reference wave at the hologram plane. (c) Hologram. (d) Image backpropagated from the hologram. (e) Image from the actual object only (ESM). (f) Image from the twin object only.

can be used at microwave frequencies if the object is illuminated by a wave produced by a generator loaded by an antenna. However, a more practical approach is to use a synthetic reference wave created by combining the signals from the reference generator and the scanning antenna [9]. The diagrams of the corresponding setup are shown in Fig. 5. In a passive DUT measurement, the reference signal could be obtained directly from the source [see Fig. 5(a)]. A more general setup uses a reference antenna configuration, which is suitable for both passive and active DUT measurement, as shown in Fig. 5(b). The reference signal needs to be coherent with the scan signal (i.e., originate from the same source) and its amplitude must be much larger than the amplitude of the scan signal. The combined signal (hologram) is measured by a SA, or even by a much simpler device, for instance, a power meter [9].

In summary, the proposed method consists of the following steps.

- 1) Setup the scan antenna and reference signal. Make sure the reference signal is much stronger than the scan signal.
- 2) Measure the field on a 2-D plane to obtain  $H(x, y, z_0)$ .
- 3) Measure or estimate the reference signal  $|R(x, y, z_0)|$ . The mean value of the hologram amplitude is used in this article as an approximation (the oscillating functions O and  $O^*$  in (6) have approximately zero mean values, therefore,  $\langle H \rangle \approx |R|^2$ ).

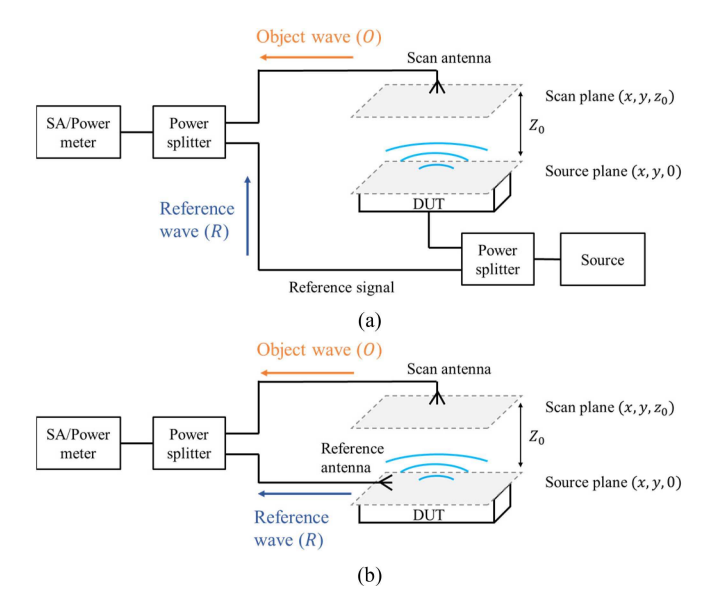


Fig. 5. Microwave holography imaging setup. The scan and reference signals can be understood as object and reference waves, respectively. (a) Imaging of passive DUTs. (b) Imaging of passive or active DUTs.

- 4) Calculate normalized hologram  $H_0(x, y, z_0)$  according to (7).
- 5) Back propagate to the source plane according to (8). Multiply with the reference signal amplitude  $|R(x,y,z_0)|$ , to obtain the absolute values of the EMI source image if needed.

The condition for successful imaging is that the reference wave is significantly stronger than the object wave  $(|R|^2 \gg |O|^2)$ . In practice, to ensure that this condition is met, the scan antenna is first connected to the receiver, and a quick manual scan is performed above the DUT at roughly the hologram plane to determine the maximum scan signal level. Afterwards, the scan antenna is replaced by the reference antenna, which is placed close to the DUT at a location where the reference signal is significantly stronger than the scan signal (the amplitude of which was estimated earlier). Based on the conducted experiments, we observed that a difference of around 10 dB is enough to achieve acceptable image quality.

As has been said previously, a larger distance between the source and hologram planes could help reducing the twin image effect, at the same time, increasing this distance reduces the signal-to-noise ratio of the normalized hologram (7). Another detrimental effect of increasing the distance to the scan plane (while maintaining the size of the scan area) is the decrease of the image resolution (see (7) in [3]).

The scan step size should be smaller than  $\lambda/2$  according to the Nyquist criterion [6].

#### III. MEASUREMENT VALIDATION

# A. Passive DUT – Antenna Source

The proposed algorithm is validated first on a passive DUT. The measurement setup is shown in Fig. 6. A horn antenna is placed at the bottom and excited by a VNA at 26 GHz. The scan

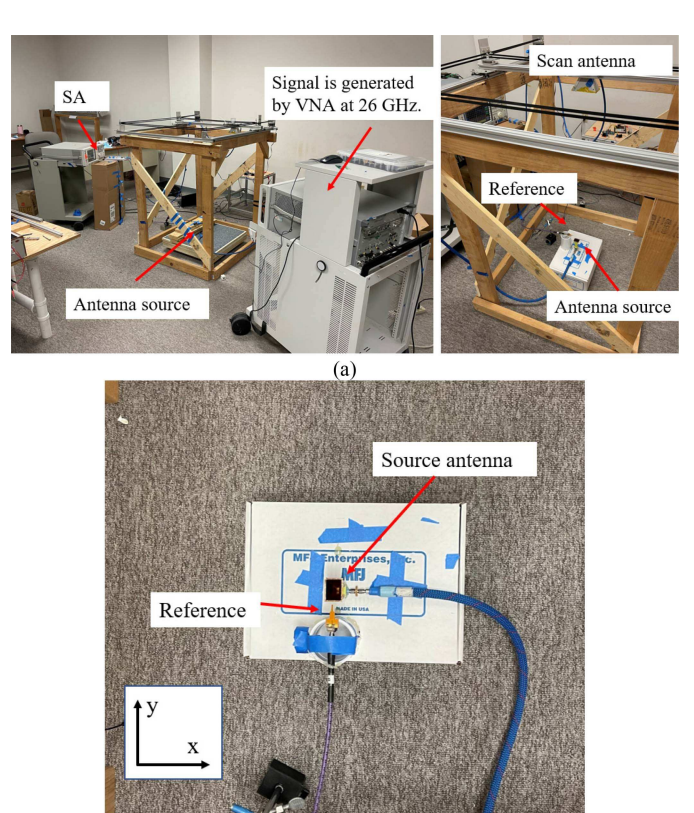


Fig. 6. Horn antenna imaging. (a) Measurement setup. (b) Top view to the scan area.

(b)

antenna is fixed on the arm of the scanner driven by two motors. The distance between the scan and the source antennas is about 70 cm. The scan area is set to  $40 \text{ cm} \times 40 \text{ cm}$ , and the step size is 4 mm. To form the hologram, a near-field probe is placed close to the source antenna to obtain the reference signal. A power splitter is used to combine the scan and reference signals. The combined signal is measured by the SA.

The measurement results are shown in Fig. 7. Fig. 7(a) demonstrates the raw data obtained from the SA. As the reference signal is much stronger than the scan signal, the hologram amplitude variations are small – less than 2 dB in this case. Since the interference pattern in the hologram has small variations, the stability of the measurement instrument may compromise the quality of the hologram. For example, a horizonal line in the hologram pattern, which can be seen in Fig. 7(a) at y = 0.27 m is the result of a sudden change (of about 0.3 dB) in the output of the SA (probably due to the SA self-calibration). However, since the information about the source is distributed over the entire area of the hologram, local defects in the hologram usually do not cause a noticeable degradation of the image quality. Fig. 7(b) shows the normalized hologram and Fig. 7(c) is the image at the source plane backpropagated and reconstructed from the normalized hologram. The peak in the center of the image represents the source antenna location. The noise in the image is mainly from the twin object effect and the diffraction of the waves on a relatively small scan aperture. Even so, the noise level is approximately 10 dB lower than the image peak.

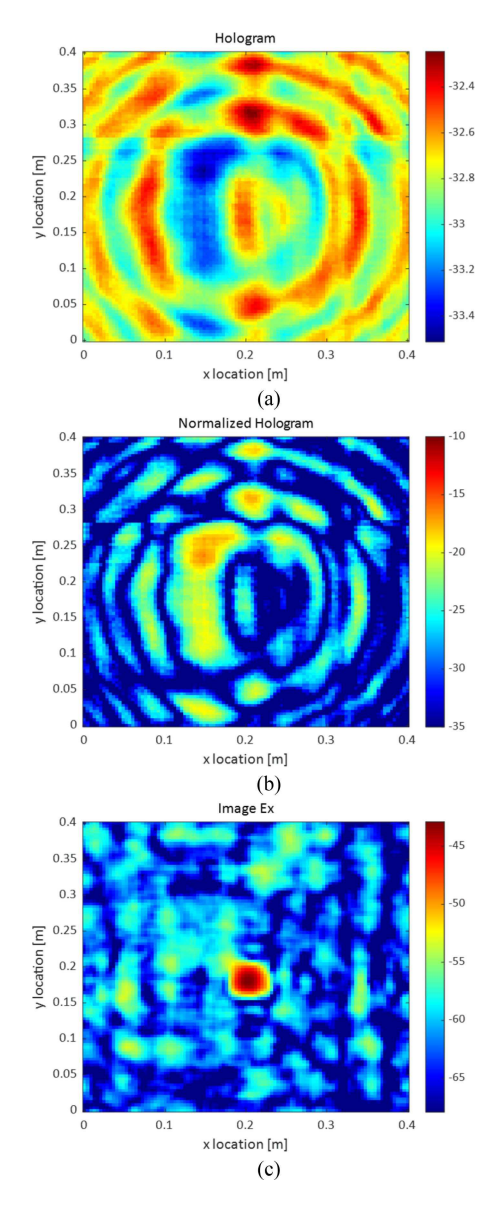


Fig. 7. Horn antenna imaging results. (a) Hologram (raw data). (b) Normalized hologram. (c) Ex Image at the source plane. Color scale in dB (arbitrary unit).

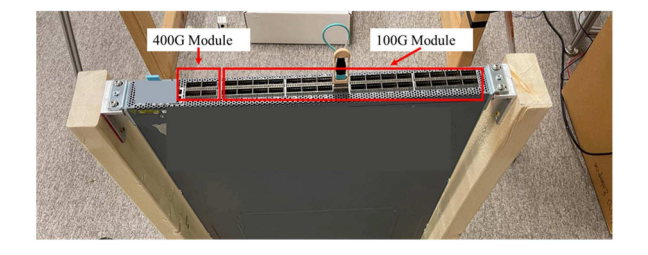


Fig. 8. Commercial router.

Overall, the algorithm is validated on the passive DUT and the radiation source is visualized and localized successfully.

## B. Active DUT – Commercial Router

In this section, holographic imaging is applied to an active DUT, a commercial network router, as shown in Fig. 8. The

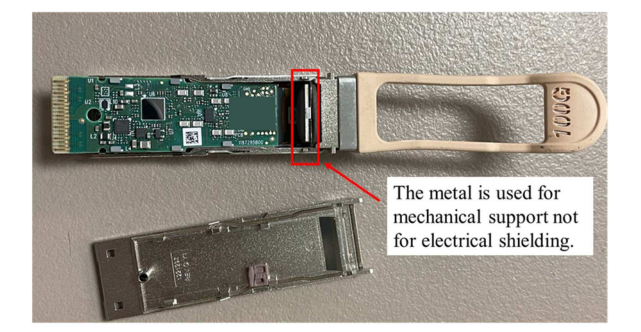


Fig. 9. Interior of an optical module.

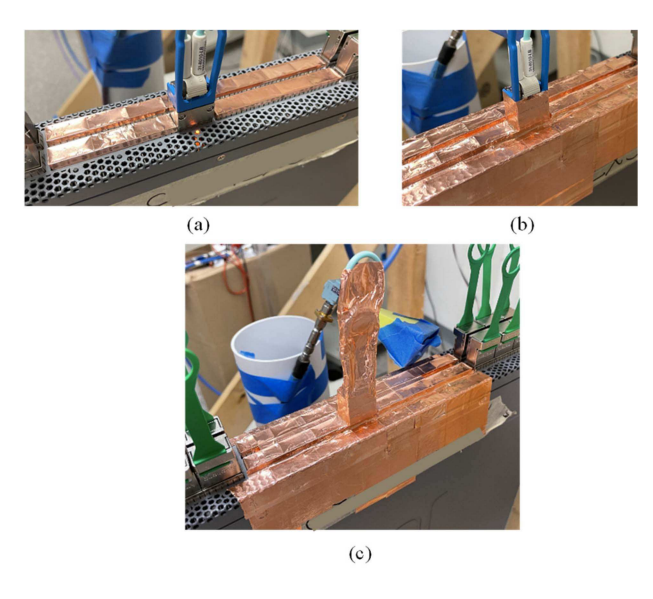


Fig. 10. Internet router imaging. (a) Case 1: Reference. One of the 100 G port is activated and adjacent ports are covered by copper tape. (b) Case 2: The gap between the module and the cage is shielded. (c) Case 3: The gap and the module are shielded.

router has 32 ports for 100 Gb/s optical modules, and 4 ports for 400 Gb/s optical modules. Only one of the 100 Gb/s port is activated in the loopback mode to create the radiation source. The measurement frequency was set to 25.78 GHz, which corresponds to the peak of the module emissions.

When the optical module is plugged to the connector, the gaps between the module and the cage could be a potential radiation source. Also, a lack of electrical shielding at the front side of the module (see Fig. 9) leads to the radiation from the module itself. To identify the radiation sources, three different cases are measured, as shown in Fig. 10. The setup in Fig. 10(a) is the reference case, where one of the 100 Gb/s port is activated, and adjacent groups of ports are covered by copper tape. Other ports are blocked by inactive electrical loopback modules. In Fig. 10(b), the gaps between the module and cage are additionally covered by copper tape. And finally in the setup in Fig. 10(c), the entire module is shielded by copper tape. The radiation level in case 3 is expected to be the lowest.

The scan area is shown in Fig. 11. A horn antenna is placed close to the active port and serves as the source of the reference signal. The distance between the face panel of the router and scan

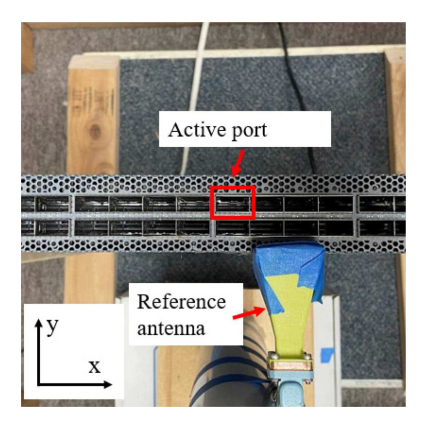


Fig. 11. Top view to the scan area. The ports adjacent to the active one are covered by copper tape in reality.

area is about 18 cm. The scan area is  $21 \text{ cm} \times 21 \text{ cm}$ , scanned with a 3 mm step. High frequency amplifiers are utilized for both scan and reference signals. Since router power-cycling or module reinsertion changes the field patterns and the EMI levels, the measurements were conducted one after another without power-cycling or module reinsertion.

The measurement results for case 1, 2, and 3 are shown in Figs. 12, 13, and 14, respectively. Both  $E_x$  and  $E_y$  components are measured and the images for both of them are created. The total tangential (to the scan plane) field is calculated as  $E_{\rm tan} = \sqrt{|E_x|^2 + |E_y|^2}$  where  $E_x$  and  $E_y$  are the component images. The radiated powers for all 3 cases are calculated, by integrating the E field over the scan area

$$P_{rad} = \int_{S} |E_{tan}|^2 ds. \tag{9}$$

It should be noted that since the scan aperture does not represent a closed surface around the DUT, the radiated power calculated this way is not equal to the total radiated power produced by the DUT and represents only a portion of it propagating through the scan aperture.

In case 1, the holograms are formed successfully, and the images show that the EMI hot spot surrounds the active port with no radiations seen above the other ports. The background noise for both  $E_x$  and  $E_y$  is 10 dB lower than the peaks. The maximum value of the EMI  $(E_{tan})$  of case 1 is -84 dB and the  $P_{rad}$  is -113.2 dB (both values are given in arbitrary units since the antenna factor, cable loss, and the amplifier gain were not compensated).

In case 2, as shown in Fig. 13, the maximum value of the EMI is reduced compared with the reference case, which points to the gap between the module and the cage as the source of radiation. However, the hot spots for both  $E_x$  and  $E_y$  are still near the module, which indicates that the shielding did not suppress the source completely. The maximum value of the EMI for case 2 is -91.9 dB, and the  $P_{rad}$  is -121.9 dB. As 7.9 dB reduction of E field and 8.7 dB reduction of  $P_{rad}$  are achieved by covering the gap between the module and the cage.

In case 3, as shown in Fig. 14, after covering the top of the module, the holograms become very noisy. This happened because the amplitude of the reference signal is close to the

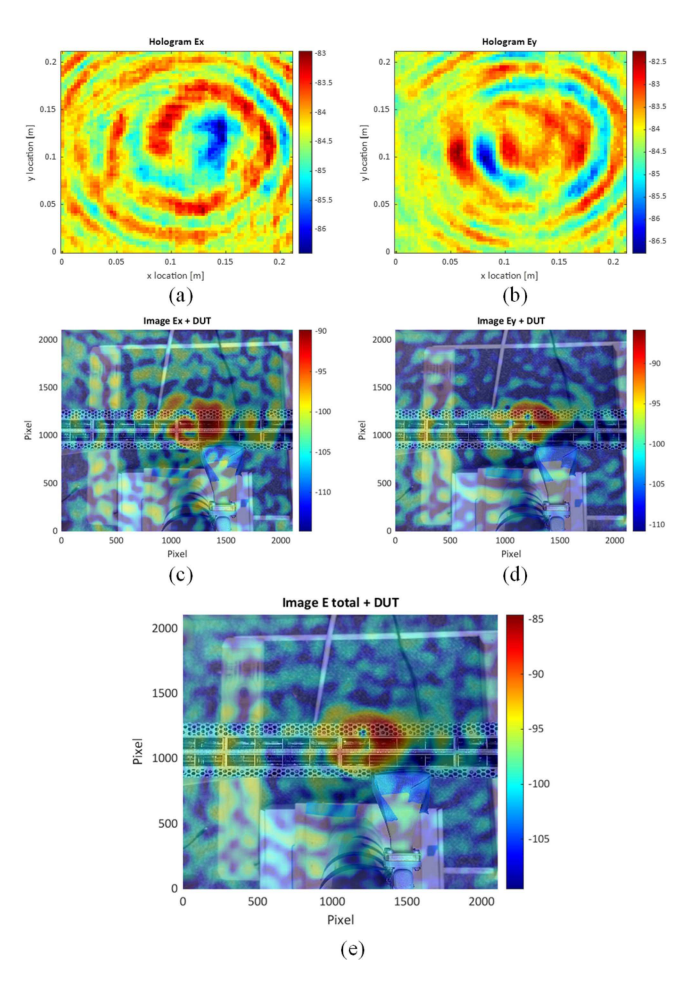


Fig. 12. Measurement results of case 1. (a) Hologram of  $E_x$ . (b) Hologram of  $E_y$ . (c) Image of  $E_x$ . (d) Image of  $E_y$ . (e) Image of E tangential. Color scale in dB (arbitrary unit).

TABLE I
MAXIMUM FIELD AND RADIATED POWER COMPARISON

Cases	Maximum E-field	$P_{rad}$	Reduction of E-field	Reduction of $P_{rad}$
1	-84.0 dB	-113.2 dB		
2	-91.9 dB	-121.9 dB	7.9 dB	8.7 dB
3	-105.6 dB	-131.6 dB	21.6 dB	18.4 dB

noise floor of the SA, and the signal from the scan antenna even falls below the noise floor. However, despite this, the images are still reasonably clean and allow to detect the residual EM leakage which happens along the front panel of the router. The maximum EMI in this case is about  $-105.6~\mathrm{dB}$  and the  $P_{rad}$  is about  $-131.6~\mathrm{dB}$ . A summary of the measurement results for 3 cases are shown in Table I. As can be seen, after the entire module is shielded by copper tape (case 3), 21.6 dB reduction of E field and 18.4 dB of  $P_{rad}$  are achieved compared with the reference case. The measurement results indicate that the gap between the module and cage and the top of the module are the main radiation sources. In conclusion, the measurement results demonstrate that the proposed algorithm is reliable in identifying major radiation sources and determining their location and relative strength.

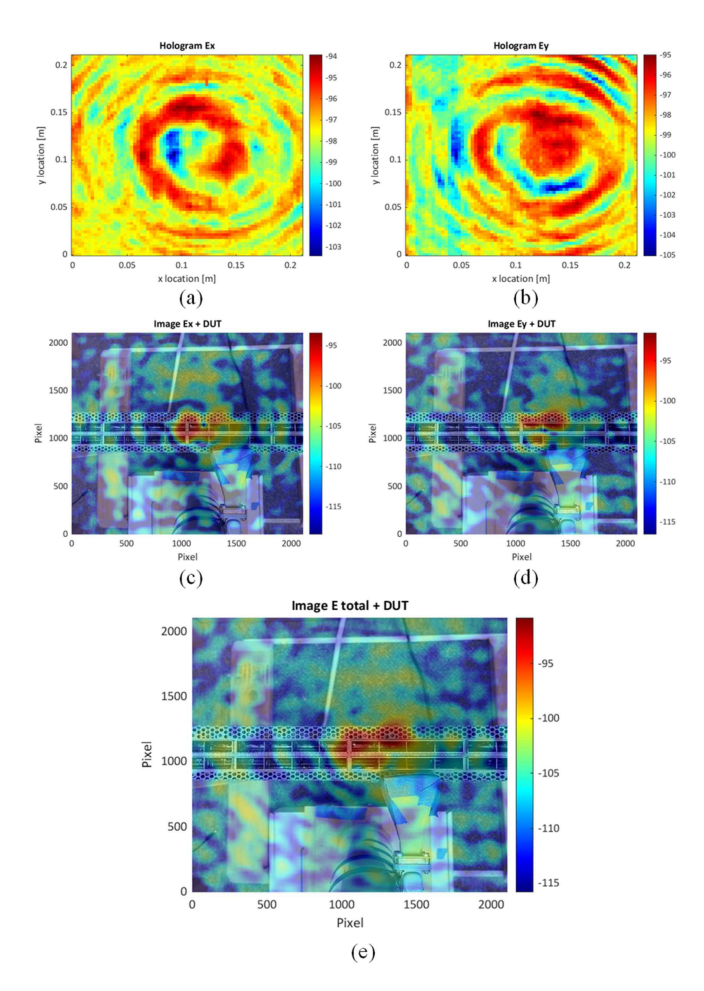


Fig. 13. Measurement results of case 2. (a) Hologram of  $E_x$ . (b) Hologram of  $E_y$ . (c) Image of  $E_x$ . (d) Image of  $E_y$ . (e) Image of E tangential. Color scale in dB (arbitrary unit).

TABLE II
MAXIMUM FIELD AND RADIATED POWER VALIDATION

Method	Maximum E-field	$P_{rad}$
ESM	-86.6 dB	-117.5 dB
Holography	-88.5 dB	-115.0 dB

To demonstrate the reliability of the holographic imaging, the images obtained holographically and by ESM imaging (with the VNA as the receiver) are shown in Fig. 15. Since router power-cycling or module reinsertion changes the field patterns and the EMI levels, the measurements were conducted immediately one after another without any change in the setup. As can be seen, the patterns and the amplitudes of the radiated sources given by the ESM and holography are very close. The accuracy of the radiated power measurement for the ESM imagining was investigated before in [3] and [4]. The maximum electric field values and the radiated power for both measurements were calculated and are given in Table II.

As can be seen, the differences between the values do not exceed 1.9 dB for the maximum field and 2.5 dB for the radiated power. It should be noted here that the presence of the twin object in holography affects both the maximum field value and

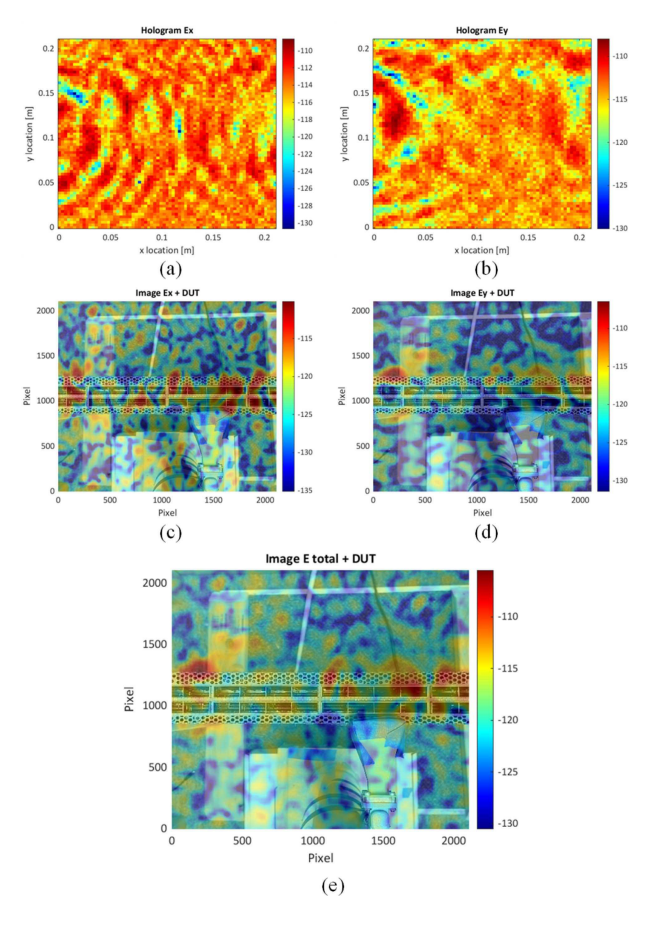


Fig. 14. Measurement results of case 3. (a) Hologram of  $E_x$ . (b) Hologram of  $E_y$ . (c) Image of  $E_x$ . (d) Image of  $E_y$ . (e) Image of E tangential. Color scale in dB (arbitrary unit).

the radiated power. And while the contribution of the twin object image to the maximum field value can be reduced by increasing the distance from the object to the hologram plane, the contribution of the twin image to the total power does not depend on this distance. Definitely, since the focusing procedure (4) does not affect the absolute value of image spectrum, its power will not be affected as well. By Parseval's theorem, the radiated power (9) can be calculated by integration of (7) on the hologram plane

$$P_{rad} = \int_{S} \left| \frac{R^*O}{|R|^2} + \frac{O^*R}{|R|^2} \right|^2 ds$$

$$= 2 \int_{S} \frac{|O|^2}{|R|^2} ds + \int_{S} \frac{(R^*)^2 O^2 + (O^*)^2 R^2}{|R|^4} ds. \quad (10)$$

The first term in (10) represents the doubled power radiated by the object, while the second one is the mutual power between the actual and twin object waves. The numerical experiments and measurement results in Table II indicate that the mutual power is close to zero and the radiated power measured holographically is two times (3 dB) higher than the actual power produced by the object. Whether or not the mutual power is close to zero under all possible conditions requires additional investigation.

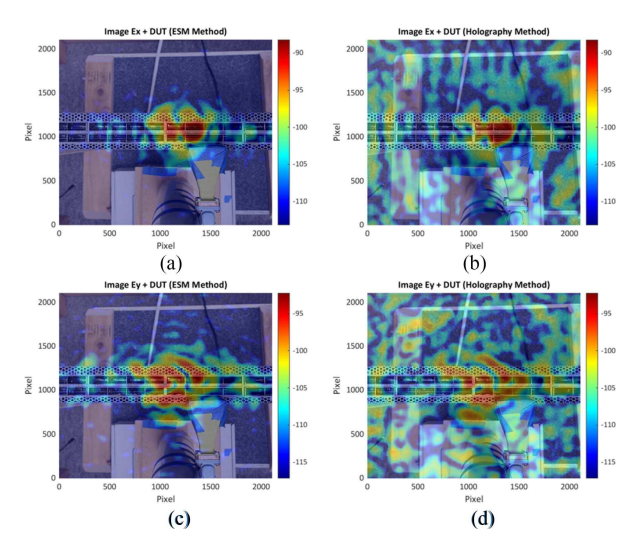


Fig. 15. Comparison between ESM and holographic imaging. (a) ESM image of  $E_x$ . (b) Holographic image of  $E_x$ . (c) ESM image of  $E_y$ . (d) Holographic image of  $E_y$ . Color scale in dB (arbitrary unit).

#### IV. CONCLUSION

In this article, we proposed a phaseless EMI source imaging method based on microwave holography, which is an alternative solution for localization and characterization of active radiation sources by measuring only the magnitude of the fields. The hologram is created by combining the signal from a scan antenna with a reference signal obtained by a stationary antenna. The normalized hologram is backpropagated to the source plane and the image of sources is reconstructed. Comparing with the traditional 2-D ESM algorithm, the twin object effect may degrade the quality of the image. On practice, however, this effect can be mitigated by increasing the backpropagation distance.

The proposed algorithm is efficient and reliable in identifying major radiation sources, determining their location and relative strength. Using the measurement setup and results shown in Fig. 15 as an example, it took 4 h to finish the scan using ESM method by VNA (Model: Keysight N5245A), as the IF bandwidth had to be reduced to 200 Hz to achieve a sufficient signal-to-noise ratio; zero-span with 250 sampling points and averaging over time samples were used to increase the measurement accuracy. In comparison, it took 40 min using the holography method by SA (Model: Agilent E4440A) with 30 Hz resolution bandwidth. In particular, when the amplitude of the radiation sources is very weak such that the measured signals are at or even below the noise level, as shown in Fig. 14, the proposed algorithm is still able to produce useful images as opposed to the ESM method, which requires a clean signal in the phase reference channel. In addition, using an SA as a receiver allows to increase the measurement sensitivity and reduces costs compared to the methods using a VNA or an oscilloscope. The future work would include calibration of the holographic method and quantitative validation of the radiated power measurement.

#### REFERENCES

 L. Zhang et al., "EMI coupling paths and mitigation in optical transceiver modules," *IEEE Trans. Electromagn. Compat.*, vol. 59, no. 6, pp. 1848–1855, Dec. 2017.

- [2] P. Maheshwari, V. Khilkevich, D. Pommerenke, H. Kajbaf, and J. Min, "Application of emission source microscopy technique to EMI source localization above 5 GHz," in *Proc. IEEE Int. Symp. Electromagn. Compat.*, 2014, pp. 7–11.
- [3] P. Maheshwari, H. Kajbaf, V. V. Khilkevich, and D. Pommerenke, "Emission source microscopy technique for EMI source localization," *IEEE Trans. Electromagn. Compat.*, vol. 58, no. 3, pp. 729–737, Jun. 2016.
- [4] L. Zhang et al., "Sparse emission source microscopy for rapid emission source imaging," *IEEE Trans. Electromagn. Compat.*, vol. 59, no. 2, pp. 729–738, Apr. 2017.
- [5] J. Li, J. Zhou, S. Yong, Y. Liu, and V. Khilkevich, "Automatic sparse ESM scan using Gaussian process regression," in *Proc. IEEE Int. Symp. Electromagn. Compat. Signal/Power Integrity*, 2020, pp. 671–675.
- [6] M. Sørensen, H. Kajbaf, V. V. Khilkevich, L. Zhang, and D. Pommerenke, "Analysis of the effect on image quality of different scanning point selection methods in sparse ESM," *IEEE Trans. Electromagn. Compat.*, vol. 61, no. 6, pp. 1823–1831, Dec. 2019.
- [7] D. Gabor, "A new microscopic principle," *Nature*, vol. 161, no. 4098, pp. 777–778, 1948.
- [8] G. Tricoles and N. H. Farhat, "Microwave holography: Applications and techniques," *Proc. IEEE*, vol. 65, no. 1, pp. 108–121, Jan. 1977.
- [9] J. L. Martínez, A. Arboleya-Arboleya, Y. Álvarez-López, C. García-González, and F. Las-Heras, "Phaseless antenna diagnostics based on off-axis holography with synthetic reference wave," *IEEE Antennas Wireless Propag. Lett.*, vol. 13, pp. 43–46, 2014.
- [10] T. Latychevskaia and H.-W. Fink, "Practical algorithms for simulation and reconstruction of digital in-line holograms," *Appl. Opt.*, vol. 54, pp. 2424–2434, 2015.



Xin Yan (Member, IEEE) received the B.S. degree in applied physics from Beihang University, Beijing, China, in 2015, and the M.S. and Ph.D. degrees in electrical engineering from Electromagnetic Compatibility Laboratory, Missouri University of Science and Technology, Rolla, MO, USA, in 2018 and 2023, respectively.

His research interests include ESD, EMI, and desense analysis.



Jiangshuai Li (Member, IEEE) received the B.S. degree in the electromagnetic technology from Huazhong University of Science and Technology, Wuhan, China, in 2019, and the M.S. degree in electrical engineering from Electromagnetic Compatibility Laboratory, Missouri University of Science and Technology, Rolla, MO, USA, in 2021.

He is currently with Apple, Austin, TX, USA, as a System SIPI Architect engineer, and previously worked in Qualcomm as a PKG SIPI engineer. His research interests include EMI/EMC, SIPI, and RFI.



Wei Zhang (Member, IEEE) received the B.S. degree in electronic information engineering from Central South University, Changsha, China, in 2014, the M.S. degree in electronic science and technology from Beihang University, Beijing, China, in 2017, and the Ph.D. degree in electrical engineering from Electromagnetic Compatibility Laboratory, Missouri University of Science and Technology, Rolla, MO, USA, in 2022.

She is currently with Marvell Technology, Wilmington, DE, USA, as a package SIPI Engineer. Her

research interests include SIPI, system EMC, and RFI.



Kaustav Ghosh received the B.E. degree in electronics and telecommunication engineering from Nagpur University, Nagpur, India, in 2012 and the master's degree in electrical engineering from Electromagnetic Compatibility (EMC) Laboratory, Missouri University of Science and Technology, Rolla, MO, USA. in 2018.

Since 2016, he has been a Graduate Research Assistant with the EMC Laboratory, Missouri University of Science and Technology. He is currently an EMC Design Engineer in Juniper Networks. His research

interests include numerical and experimental study of EMI problems at system level and board level, power supply EMC, analysis of EMI emission issues, and different EMI mitigation techniques.

Mr. Ghosh is a member of the IEEE EMC society.



Daryl G. Beetner (Fellow, IEEE) received the B.S. degree in electrical engineering from Southern Illinois University, Edwardsville, IL, USA, in 1990, and the M.S. and D.Sc. degrees in electrical engineering from Washington University, St. Louis, MO, USA, in 1994 and 1997, respectively.

He was employed with the Missouri University of Science and Technology, Rolla, MO, USA (Missouri S&T), where he is a Professor of electrical and computer engineering and was the former Department Chair. He is the Director with the Missouri

S&T Electromagnetic Compatibility Laboratory, and is the Director with the Center for Electromagnetic Compatibility, National Science Foundation Industry/University Cooperative Research Center.

Dr. Beetner was the recipient of 2020 the IEEE Electromagnetic Compatibility (EMC) Society Technical Achievement Award and the 2003 IEEE-HKN C. Holmes MacDonald Outstanding Young Electrical Engineering Professor, and has won a number of best paper awards including the 2018 Richard B. Schulz Best Transaction Paper award honorable mention. He is currently the IEEE EMC Society as the EMC Education Grants Chair, the Chair of TC-4 Electromagnetic Interference Control, and as a member of the EMCS Board of Directors. He is the Chair of the selection committee for the IEEE Medal for Environmental and Safety Technologies, as a member of the IEEE Medals committee, and as a member of the IEEE-HKN Outstanding Young Professional committee.



Philippe Sochoux received the B.S. and M.S. degrees in electrical engineering from Marquette University, Milwaukee, WI, USA, in 1990 and in 1994, respectively.

He is currently a Senior Manager with the Electromagnetic Compatibility (EMC) Design with Juniper Networks, Sunnyvale, CA, USA. Prior to joining Juniper, he was managing Compliance (EMC, Mechanical Design Verification Testing, Safety, System Optical Design Verification Testing, and Network Equipment Building Systems) as well as Signal In-

tegrity with Cisco Systems.



**Victor Khilkevich** (Senior Member, IEEE) received the Ph.D. degree in electrical engineering from the Moscow Power Engineering Institute, Technical University, Moscow, Russia, in 2001.

He is currently a Research Professor with the Missouri University of Science and Technology, Rolla, MO, USA. His research interests include signal processing, microwave structures design and analysis, electromagnetic simulation, signal integrity, timedomain measurement of network parameters, near-field scanning, electromagnetic field transformation,

measurement and processing of random signal and fields, EMI mitigation techniques, EMI source and coupling path identification, and microwave imaging.